Fractal complexity of Escherichia coli nutrient transport channels is influenced by cell shape and growth environment

Beatrice Bottura[1], Liam Rooney[2], Morgan Feeney[2], Paul A. Hoskisson[2], Gail McConnell[2]

[1] Department of Physics, SUPA, University of Strathclyde, G4 0NG, Glasgow, UK
[2] Strathclyde Institute of Pharmacy and Biomedical Sciences, University of Strathclyde, G4 0RE, Glasgow, UK

Recent mesoscopic characterisation of nutrient-transporting channels in *E. coli* has allowed the identification and measurement of individual channels in whole mature biofilms. However, their complexity under different physiological and environmental conditions remains unknown. Analysis of confocal micrographs of biofilms formed by cell shape mutants of *E. coli* shows that channels have a high fractal complexity, regardless of cell phenotype or growth medium. In particular, biofilms formed by the mutant strain Δ*ompR*, which has a wide-cell phenotype, have a higher fractal dimension when grown on rich medium than when grown on minimal medium, with channel complexity affected by glucose and agar concentration in the medium. Osmotic stress leads to a dramatic reduction in Δ*ompR* cell size, but has a limited effect on channel morphology. This work shows that fractal image analysis is a powerful tool to quantify the effect of phenotypic mutations and growth environment on the morphological complexity of internal *E. coli* biofilm structures. If applied to a wider range of mutant strains, this approach could help elucidate the genetic determinants of channel formation in *E. coli* biofilms.

1. Introduction

The formation of spatial patterns is ubiquitous in biological systems, where discrete entities come together to form complex structures in a process called "morphogenesis" [1]. Bacterial populations are no exception to this phenomenon: bacterial biofilms exhibit a variety of internal patterns, from surface and 3D features to complex fractal shapes [2]. Fractal geometry has previously been proposed as a tool for the investigation of microbial growth patterns [3], and it has since been employed to quantify biofilm morphology from microscopy images [4]–[6], to describe colony morphogenesis in Gram-negative rod-shaped bacteria [7] and to analyse nutrient-limited growth patterns [5], [8].

In *E. coli*, fractal patterns mostly exist within cellular aggregates of co-cultured isogenic strains expressing different fluorescent makers [9] [10]. Fractal boundaries are formed during uniaxial cell growth and division, and can be a result of local instabilities [11]. Alternatively, fractal domains can be observed between mutant sectors arising from genetic differences in the population [12], where mutants with a fitness advantage grow faster and gain greater access to nutrients at the periphery of the colony [13]. Metabolic interactions between isogenic strains can lead to different patterns of self-organisation, from uniform radial expansion to the formation of dendritic niches at the colony edge [14].

37   Fractal boundaries have also been observed in *E. coli* cocultures of cross-feeding strains, where the type
38   of social interaction determines the level of spatial mixing between the two strains [15]. The degree of
39   self-similarity across the boundaries, usually measured through the fractal dimension, depends on the
40   properties of the constituent cells.

41   The network of nutrient-transporting channels in *E. coli* biofilms [16] also exhibits a complex 3D
42   morphology. The spatial structure of these emergent channels bears a striking resemblance to the
43   fractal boundary patterning described in multi-strain co-culture biofilms, although these channels are
44   not occupied by cells. In previous work, we measured the width of individual channels at different
45   locations within the biofilm and showed that the channel architecture is affected by environmental
46   growth conditions [17], but a quantification of channel morphology at the whole-biofilm scale has not
47   been performed to date.

48   In this study, we quantify the morphological complexity of *E. coli* nutrient-transporting channels using
49   fractal analysis of confocal microscopy images of biofilms. We hypothesised that their fractal nature
50   would be affected by the shape of the constituent cells, because channel formation is an emergent
51   property of biofilm growth. To test this hypothesis, we selected three *E. coli* mutant strains with altered
52   cell shape phenotypes for morphological analysis. We show that the internal patterns formed by
53   nutrient-transporting channels in *E. coli* have a fractal complexity comparable to that of computer-
54   generated fractal images, and that this complexity is affected by cell shape and growth medium. We also
55   report the specific case of Δ*ompR*, a wide-cell mutant whose biofilm morphological complexity is
56   particularly affected by growth medium composition.

57

2. Results

## 2.1.   Cell shape affects biofilm morphology

60   The single knockout mutants Δ*amiA*::kan, Δ*ompR*::kan and Δ*ydgD*::kan of the *E. coli* strain BW25113,
61   hereby referred to as Δ*amiA*, Δ*ompR* and Δ*ydgD,* were chosen from the Keio collection for their altered
62   cell shape phenotype (long, wide and wide respectively). The length and width of individual segmented
63   cells were calculated for each strain from phase-contrast microscopy images (Supplementary Figure 1)
64   and compared to the measurements of the isogenic parental strain BW25113 for quantitative
65   phenotypic analysis. Δ*amiA* cells were on average 34% longer than the parental strain, whereas Δ*ompR*
66   and Δ*ydgD* cells were on average 48% and 23% wider than the parental strain respectively.

67   After single-cell phenotypic characterisation, the three mutant strains were grown into mature biofilms
68   on both LB (rich) and M9/glucose (minimal) solid growth medium (Figure 1). Confocal microscopy of
69   these biofilms revealed a complex network of intra-colony channels, as previously reported for *E. coli*
70   JM105 [16], [17]. Biofilms formed on minimal medium exhibited sectoring, with large areas of low
71   fluorescence intensity across the biofilm volume, and channels appeared less morphologically complex
72   than in their rich medium counterparts. This was particularly evident in the Δ*ompR* strain, where
73   channels expand radially outwards in approximately straight lines, reminiscent of strain boundaries
74   observed between isogenic domains in biofilms formed by spherical mutants of *E. coli* [11]. On rich
75   medium, channels had more complex arrangements - in particular, channels formed by the Δ*amiA* strain
76   were made up of long (≥ 10 μm) segments, consistent with the long cell phenotype of the constituent

77 cells. Channels formed by the Δ*ompR* mutant strain, on the other hand, appeared fragmented, likely
78 owing to the constituent cells' irregular morphology.

79 Furthermore, despite both Δ*ompR* and Δ*ydgD* strains having a wide cell phenotype, their biofilms had
80 different internal morphologies, especially on rich medium. Here Δ*ompR* formed darker channels, which
81 were clearly distinguishable from the surrounding cells within the biofilm. On minimal medium, the
82 central region of Δ*ydgD* biofilms appeared devoid of channels, whereas the edges showed radially
83 expanding channels highly similar to those observed at the edges of Δ*ompR* biofilms. Enlarged regions of
84 interest showing channel morphology are shown in Supplementary Figure 2.
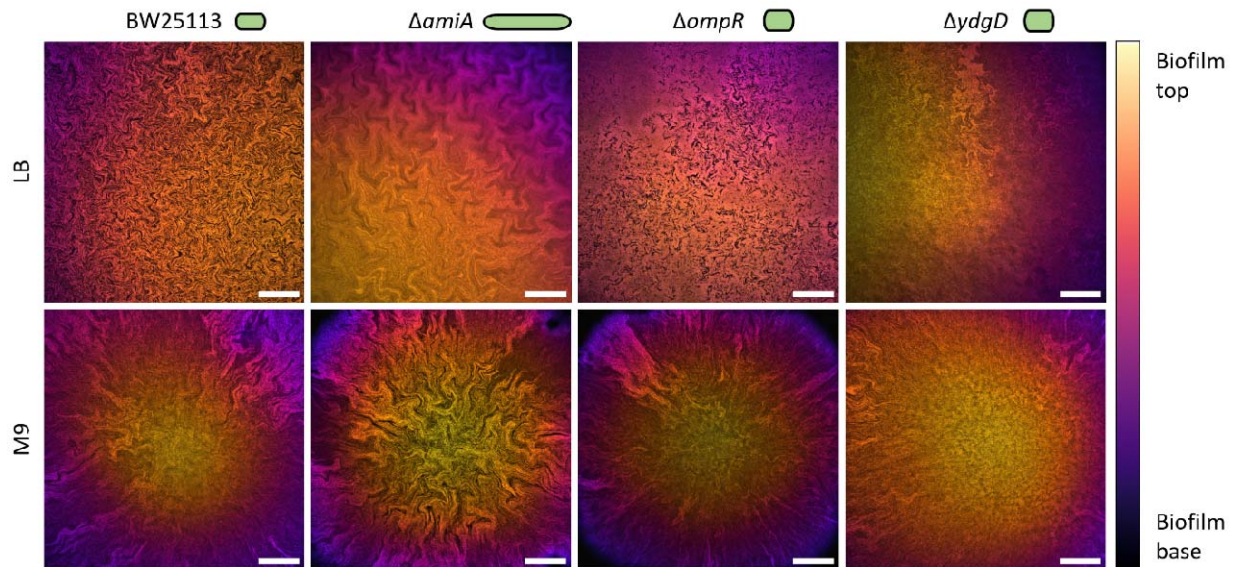
85

86 Figure 1: Representative confocal microscopy images showing the morphology of biofilms formed by the strains
87 BW25113, Δ*amiA*, Δ*ompR* and Δ*ydgD* when growing on LB (rich) or M9 (minimal) solid medium. Images are
88 projections of z-stacks acquired with 5 μm slice spacing, colour-coded by depth. The cell phenotype of each strain
89 is shown as a green cartoon for reference. Scale bars: 200 μm.

90

2.2. Internal channel patterns in *E. coli* biofilms are fractal

92 The fractal complexity of internal biofilm patterns was quantified using relative differential box-counting
93 (RDBC) dimension, which was calculated using the open-source plugin ComsystanJ on FIJI. Firstly, the
94 plugin was used on four sets of computer-generated images with increasing spatial complexity (as
95 described in the Methods), to obtain a correlation between visual complexity and RDBC dimension
96 (Figure 2). Constant images had a RDBC dimension of 0 due to the lack of spatial features, whereas the
97 RDBC dimension of images comprised of straight lines ranged between 2.114 ± 0.032 and 2.213 ± 0.043
98 (mean ± standard deviation). The RDBC dimension for computer-generated fractal images were
99 calculated as between 2.329 ± 0.041 and 2.702 ± 0.047, and images of randomized features had a RDBC
100 dimension equal to 2.959, close to the theoretically possible maximum of 3.000.

101
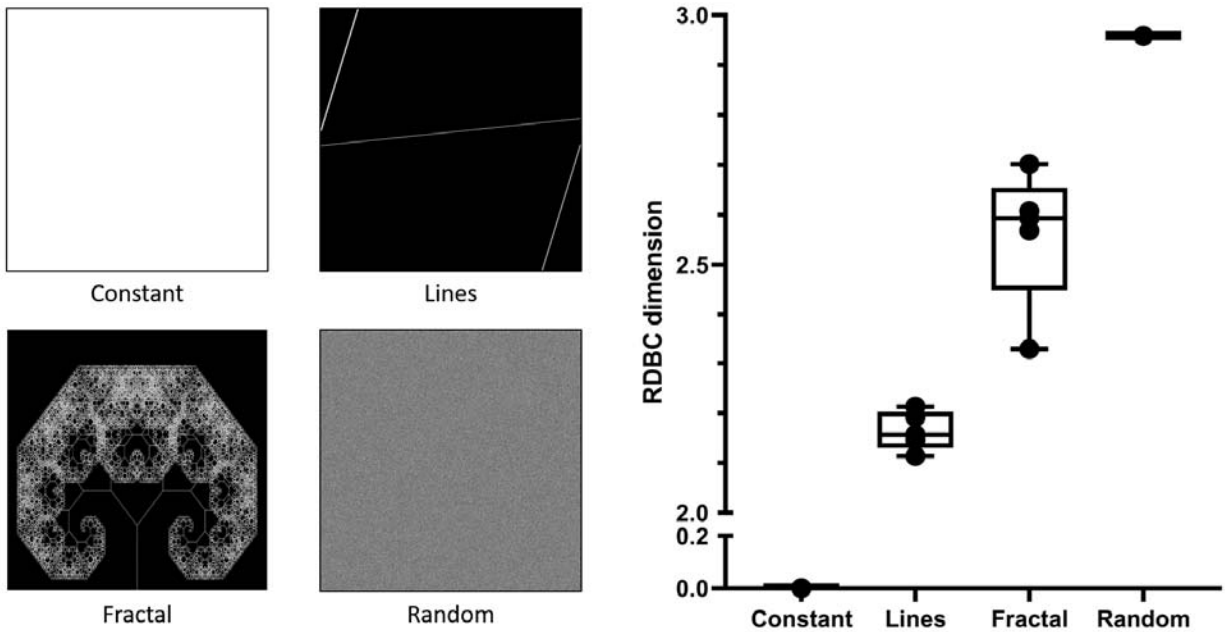
102

103   Figure 2: Representative images from the sets used for benchmarking of RDBC calculations (right panel). Each set
104   consists of five images, whose fractal complexity is calculated using ComsystanJ. The constant, lines, and random
105   images were generated in ComsystanJ, whereas the fractal images were obtained from open-source image
106   repositories. Increasing complexity in the image sets is reflected by an increase in relative differential box-counting
107   dimension, which ranges between 2.329 ± 0.041 and 2.702 ± 0.047 for fractal images.

108   After obtaining benchmark values for fractal complexity, confocal microscopy images of biofilms were
109   analysed using the same image analysis pipeline to investigate the effect of cell shape and growth
110   medium on the complexity of internal biofilm patterns (Figure 3). RDBC dimension values obtained from
111   biofilm images fully aligned with those calculated for the set of computer-generated fractal images, with
112   a minimum of 2.488 and a maximum of 2.620. This confirmed that channel structures in *E. coli* biofilms
113   could be described using fractal geometry.

114   On rich medium, biofilms formed by the Δ*amiA* mutant strain showed increased fractal complexity
115   (RDBC = 2.578 ± 0.009) when compared to biofilms formed by Δ*ydgD* (RDBC = 2.553 ± 0.009, p = 0.0277).
116   This reflects the peculiar channel architecture exhibited by Δ*amiA* biofilms grown on LB medium (Figure
117   1). On minimal medium, the parental strain BW25113 formed more complex biofilms (RDBC = 2.581 ±
118   0.014) than the Δ*ompR* mutant (RDBC = 2.522 ± 0.011, p = 0.0005). Biofilms formed by the mutant
119   Δ*ydgD* were also less complex (RDBC = 2.576 ± 0.028) than those formed by Δ*ompR* (p = 0.0013), despite
120   both strains having the same wide cell shape phenotype.

121   As shown in the image data presented in Figure 1, growth on minimal media was objectively correlated
122   with large, dark sectors within the biofilm, which we hypothesised would result in a lower fractal
123   complexity. However, after quantifying channel morphology through RDBC dimension and comparing
124   each strain grown on the two different growth media we observed no statistical difference. An
125   important exception to this observation was the Δ*ompR* mutant strain, for which growth in minimal
126   medium was associated with significantly lower morphological complexity than growth in rich medium
127   (p = 0.0008). This finding is investigated in more detail in the following sections.

128
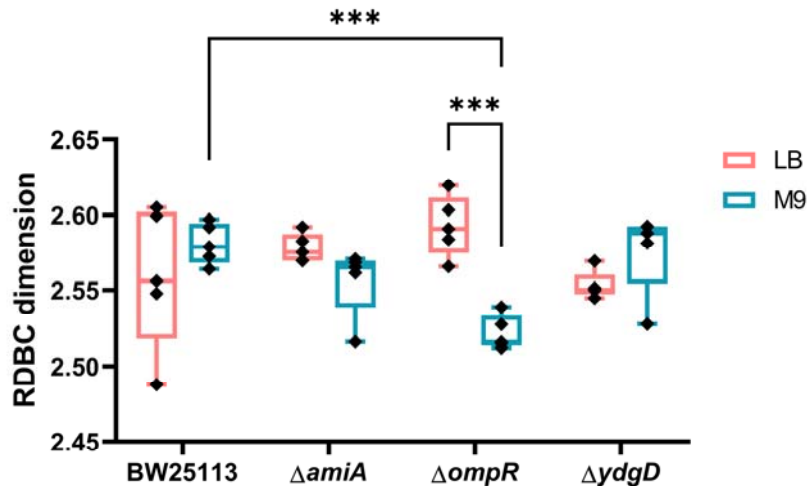
Figure 3: Box-counting dimension calculated from confocal micrographs of biofilms (n = 5 for each condition). On minimal medium (M9), biofilms formed by the ΔompR mutant strain are less morphologically complex than those formed by the parental strain (p = 0.0005). For the ΔompR mutant strain, the fractal complexity is also strongly affected by the growth substrate composition, with biofilms grown on rich medium (LB) showing significantly more complexity than those grown on minimal medium (M9, p = 0.0008). Average values are compared using one-way ANOVA tests.

2.3.   Growth medium composition affects the complexity of ΔompR biofilms

We further investigated the role of medium composition on ΔompR biofilm internal morphology by comparing biofilms grown on LB and M9 substrates with different chemical compositions (Figure 4). The RDBC dimension of biofilms grown in rich medium decreased considerably when the substrate was made softer by halving the amount of agar (p = 0.0117). On minimal medium, on the other hand, growth on soft (1% agar) substrates was associated with a significant increase in RDBC dimension, comparable to that of biofilms grown on rich medium (p = 2.39 $\times$ 10^{-7}).

Furthermore, increasing glucose amounts in minimal medium led to an increase in RDBC from 2.376 ± 0.007 (0.02% glucose) to 2.503 ± 0.032 (0.2% glucose, p = 4.81 $\times$ 10^{-11}) to 2.543 ± 0.005 (0.5% glucose, p = 0.0478). In ΔompR, this increase in RDBC dimension coincided with the gradual disappearance of colony sectoring, brought by the increase in nutrient levels. As expected, the addition of the same amounts of glucose to rich medium did not lead to any significant changes in biofilm morphological complexity, with RDBC dimensions (2.520 < RDBC < 2.622) comparable to those found in nominal rich medium with no glucose (2.566 < RDBC dimension < 2.620).

While the diameter of ΔompR biofilms increased with glucose concentration and decreased with agar concentration, the presence of dark background in images of smaller biofilms did not significantly affect the resulting RDBC dimension. This was checked by digitally zooming into images of the biofilms grown on 0.02% glucose (which had the smallest base area) until they filled the field of view of the images, and by successively calculating their RDBC dimension. The resulting RDBC value was calculated as 2.373 ± 0.006, a decrease of only 0.1% compared to the original biofilm images (Supplementary Figure 3).
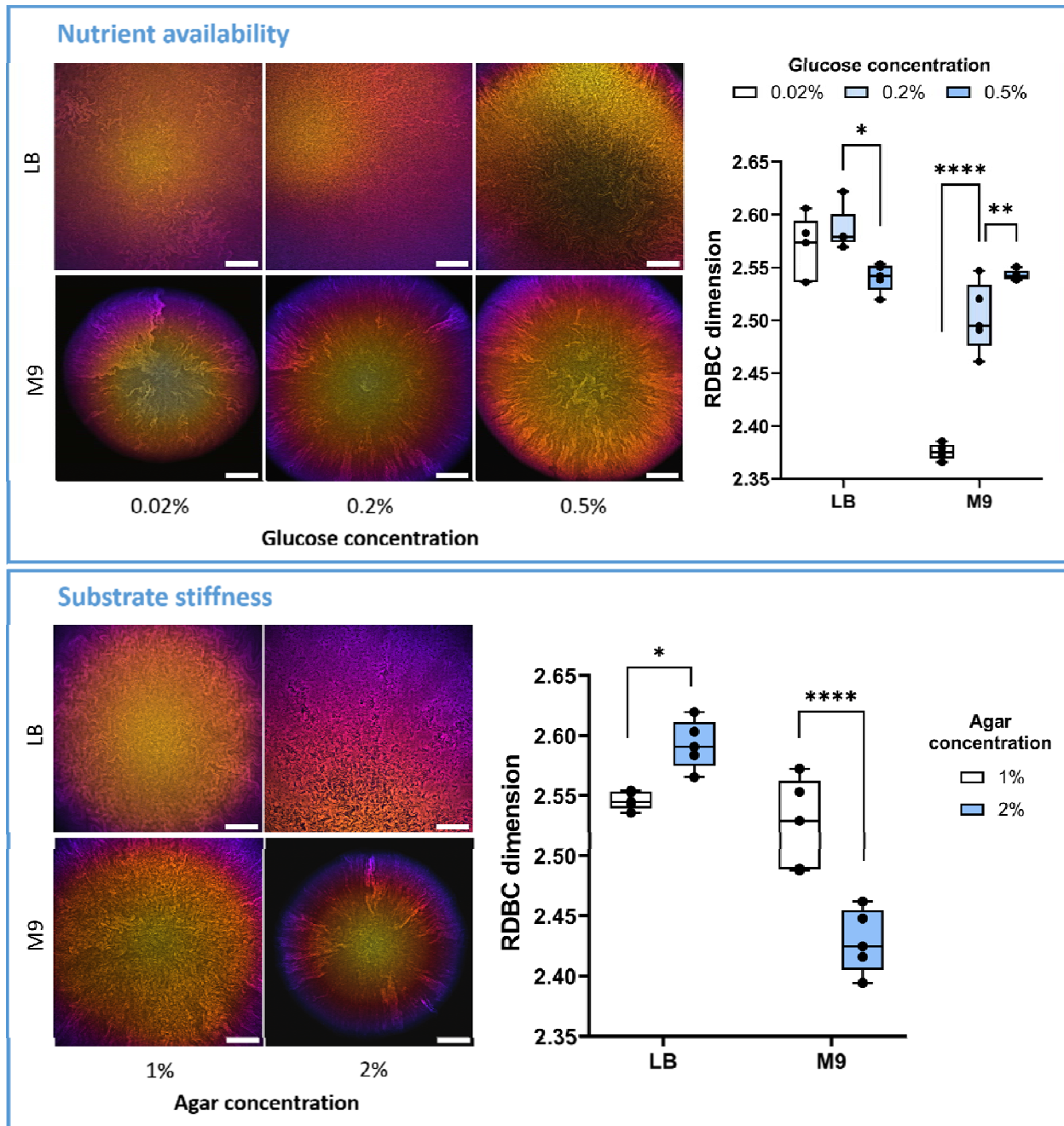
Figure 4: Morphology and fractal complexity of biofilms formed by the Δ*ompR* mutant strain grown on solid substrates with different glucose and agar concentrations. Glucose concentration in the medium is particularly important for the complexity of biofilms grown on minimal media (M9): RDBC dimension increases when glucose levels are increased from 0.02% to 0.2% ($p = 4.81 \times 10^{-11}$) and from 0.2% to 0.5% ($p = 0.0478$). On rich medium (LB), conversely, the addition of glucose does not significantly affect biofilm fractal complexity: only a small reduction in RDBC dimension is observed between 0.2% and 0.5% added glucose ($p = 0.0166$). Finally, a reduction in substrate stiffness from 2% to 1% agar concentration leads to a decrease in complexity on rich medium ($p = 0.0365$) and an increase in complexity on minimal medium ($p = 2.39 \times 10^{-7}$). Average values are compared using one-way ANOVA tests. Scale bars: 200 μm.

2.4.   Osmotic stress partially reduces biofilm complexity in Δ*ompR*

Because of the role of *ompR* in osmotic stress response, the fractal complexity of biofilms formed by the mutant strain Δ*ompR* was studied on LB and M9/glucose medium with and without salt (Figure 5). A reduction in RDBC dimension was observed when the osmolality of the medium was reduced by removing salt, both in rich medium (p = 4.88 $\times$ 10^{-5}) and in minimal medium (p = 0.0209). This suggested that osmotic stress might control the morphology of biofilms formed by the Δ*ompR* mutant strain.
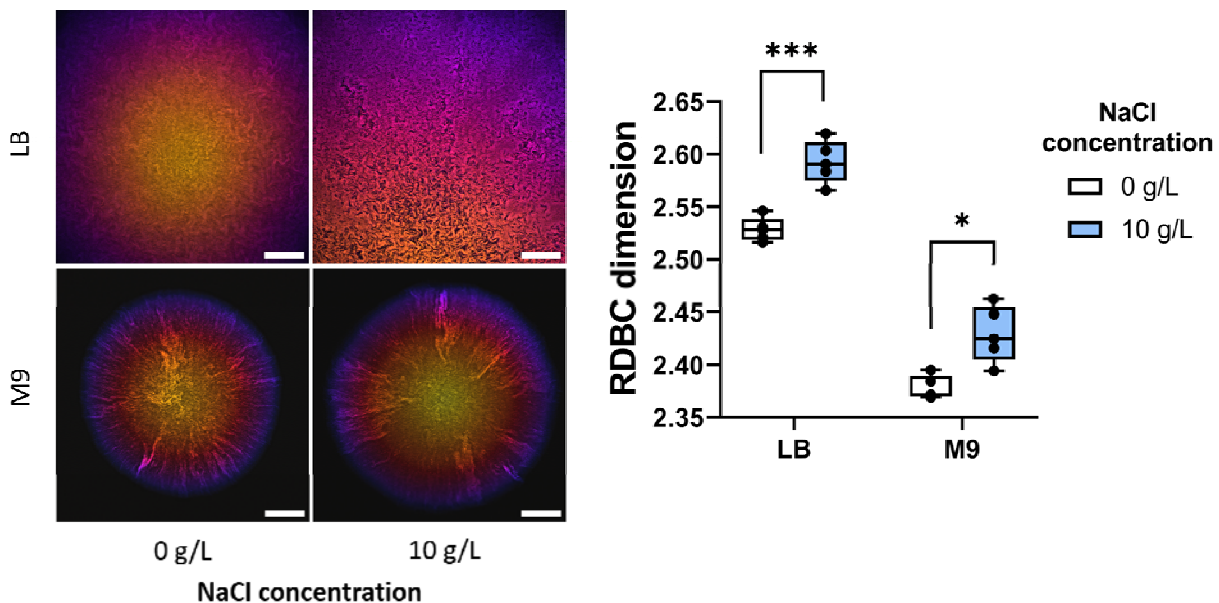
Figure 5: Morphology and fractal complexity of biofilms formed by the Δ*ompR* mutant strain grown on LB and M9/glucose solid substrates with and without NaCl. The presence of 10 g/L NaCl is associated with an increase in biofilm morphological complexity for both rich and minimal media (p = 7.34 $\times$ 10^{-4} and p = 0.0209 respectively), as indicated by the RDBC dimension metric.

For this reason, the role of osmotic stress on the growth of the Δ*ompR* mutant strain was investigated at both the cellular level and at the biofilm level. This was achieved by measuring changes in cell length and width and by measuring the RDBC dimension of biofilm images grown in solid media with different osmolalities, respectively. Changes in growth medium osmolality were induced by adding different amounts of iodixanol, a compound originally designed for density gradient preparations that cannot be metabolised by the bacteria [18]. Iodixanol toxicity in both the parental strain BW25113 and the Δ*ompR* mutant was checked by growth curve experiments (Supplementary Figure 4). At the cellular level, an increase in osmotic stress in the liquid growth media led to a reduction in cell size for both strains (Supplementary Figure 5). A significant reduction in cell length with increasing iodixanol concentration was observed in both strains: from 3.520 ± 0.827 µm to 2.205 ± 0.516 µm for BW25113 (p = 1.32 $\times$ 10^{-167}), and from 3.878 ± 1.133 µm to 2.685 ± 0.657 µm for Δ*ompR* (p = 6.74 $\times$ 10^{-40}). By contrast, cell width reduction with increasing iodixanol concentration was marginal for BW25113 (from 1.001 ± 0.099 µm to 0.970 ± 0.098 µm, p = 8.57 $\times$ 10^{-8}), whereas it was almost five times higher for the Δ*ompR* strain (from 1.335 ± 0.219 µm to 1.147 ± 0.149 µm, p = 1.02 $\times$ 10^{-13}).

194 In biofilms, an increase in iodixanol concentration in the solid growth substrate was associated with a
195 small overall reduction in RDBC dimension for both strains (Figure 6). This loss of internal complexity
196 could occur because planktonic growth is limited in high osmolality medium (Supplementary Figure 4),
197 or it could be a result of the cell size reduction following osmotic stress (Supplementary Figure 5).
198 Alternatively, it could be a pleiotropic effect caused by the presence of iodixanol in the growth medium.

199
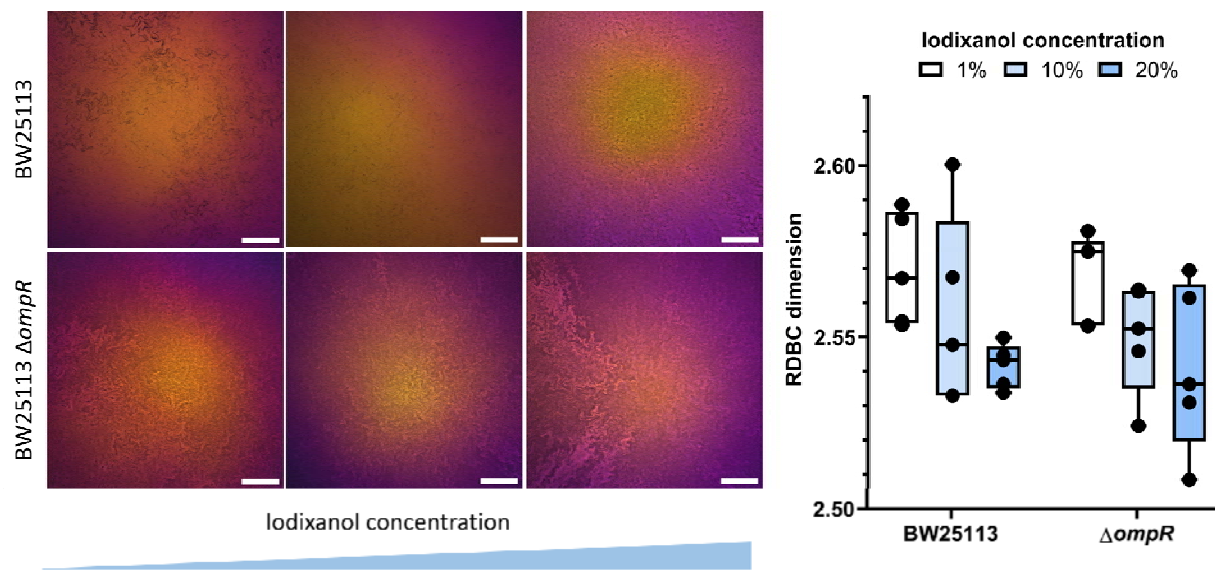
200

201 Figure 6: Comparison of fractal morphology between biofilms formed by the parental strain BW25113 and the
202 mutant strain Δ*ompR* on solid substrates with increasing iodixanol concentrations (1%, 10% and 20% v/v). Biofilm
203 images are colour-coded by depth. Average RDBC dimension decreases with increasing amounts of iodixanol and is
204 similar between the two strains for each iodixanol concentration. Scale bars: 200 μm.

205

3. Discussion

207 The formation of intra-colony channel networks is an emergent property of *E. coli* biofilms, where these
208 channels constitute a novel nutrient uptake system [16]. The chemical makeup of the growth
209 environment is known to affect the density and the size of these channels within the biofilm [17],
210 however the factors controlling channel morphogenesis are currently unknown. A method for the
211 systematic, quantitative characterisation of channel morphology is therefore needed to elucidate the
212 mechanisms governing channel formation.

213 In this study, we analysed the effect of cell shape mutations and growth medium composition on the
214 morphological complexity of *E. coli* biofilms using confocal microscopy and image analysis. We showed
215 that the fractal morphology of *E. coli* nutrient transport channels was comparable to that of computer-
216 generated fractals for all cell shape mutants and growth conditions. While cell shape affected the overall
217 biofilm morphology, this did not lead to a significant change in fractal complexity, as described by the
218 RDBC dimension metric. However, the wide-cell mutant strain Δ*ompR* formed biofilms with a higher
219 RDBC dimension on nutrient excess than on nutrient limited conditions.

220   To investigate the cause of this phenomenon, we examined the effect of growth medium composition
221   on ΔompR biofilm fractal complexity. We found that glucose concentration was particularly important in
222   minimal medium, where it constituted the sole carbon source. Increasing glucose concentrations in
223   minimal medium led to proportionally more complex biofilm channel organisation, eventually reaching a
224   RDBC dimension value close to that of biofilms grown on rich media. A similar effect was previously
225   observed in E. coli JM105 mini-Tn7-gfp biofilms, which developed more complex channel patterns when
226   grown on minimal medium with an excess of glucose compared to glucose-limited substrates [17].
227   Furthermore, we found that growth on rich soft substrates reduced biofilm morphological complexity,
228   whereas growth on soft minimal substrates increased it. This is in contrast with previous findings on E.
229   coli JM105 mini-Tn7-gfp, where channels from biofilms grown on rich, soft substrates were densely
230   packed [17].

231   We investigated the morphology of ΔompR cells and biofilms under growth conditions with varying
232   osmolality owing to the role of OmpR in regulating the osmotic stress response in E. coli [19]. Gram-
233   negative bacteria such as E. coli respond to an increase in external osmotic pressure by accumulating
234   solutes inside the cell, and by pumping out water through efflux [20]. Hyperosmotic shock also leads to a
235   sudden cell volume shrinkage [21], followed by a gradual recovery [22], and is associated with a
236   reduction in cell elongation rate [23]. We investigated the effect of medium osmolality on biofilm
237   morphology by comparing RDBC dimension values between biofilms grown on solid substrates with and
238   without NaCl, and we found that low osmolality was associated with a lower fractal complexity on both
239   rich and minimal media. Because NaCl affects not only medium osmolality, but also nutrient metabolism
240   [24], we then used iodixanol for subsequent osmotic stress experiments. The observed reduction in
241   ΔompR cell width in high osmolality medium indicates a possible partial reversion to the parental
242   phenotype, which could equally be driven by ompR suppressor mutations. This phenotypic reversion in
243   cell shape may also explain the similarity in absolute RDBC dimension values between BW25113 and
244   ΔompR biofilms at each iodixanol concentration.

245   The extraction of fractal geometry parameters from biofilm micrographs (see for example [25]) is usually
246   achieved by image thresholding, a type of image segmentation which isolates an object from its
247   background depending on its grayscale value [26]. While this method can accurately identify biofilm
248   outlines, it is not effective for the detection of internal channel networks, where difference in grayscale
249   values between the channels and the rest of the biofilm is small. In our work, this obstacle is overcome
250   using the fractal analysis software ComsystanJ. The use of fractal geometry has proven to be a simple
251   yet powerful method for the quantification of E. coli biofilm internal channels formed by cell shape
252   mutants on different growth substrates. Our analysis could help identify the factors controlling the
253   formation and development of nutrient-transporting channels in E. coli, and it could be readily applied
254   to other microbial species exhibiting complex biofilm internal patterns.

255

4. Materials and methods

4.1.   Strains and media

258   The bacterial strains used in this work (Supplementary Table 1) were obtained from the Keio collection
259   [27], a single-gene knockout library of all nonessential genes in the E. coli K-12 strain, BW25113 [28]. The
260   mutants ΔamiA::kan, ΔompR::kan and ΔydgD::kan of the E. coli strain BW25113, hereby referred to as

261 Δ*amiA*, Δ*ompR* and Δ*ydgD*, were selected for their modified cell phenotype, and their single-gene
262 deletions were verified by PCR and DNA amplicon sequencing (Supplementary Table 2). The strains were
263 transformed by electroporation with the plasmid pAJR145, which is derived from the plasmid pACYC184
264 and encodes the constitutively-expressed green fluorescent protein (GFP) transcriptional fusion
265 *rpsM::gfp+* [29]. Prior to transformation, liquid cultures of each strain were made electrocompetent
266 through three ice-cold 10% glycerol washes.

267 Liquid cultures were grown overnight in a 37°C aerated incubator while shaking at 250 rpm, in Miller
268 Lysogeny Broth (LB) [30] with the addition of 25 µg/mL chloramphenicol to maintain GFP fluorescence
269 from the pAJR145 plasmid. Keio mutant strains were also grown with the addition of 50 µg/mL
270 kanamycin. M9 minimal medium salts [30] were prepared as a 5× solution, then diluted to 1× with
271 distilled deionised water and supplemented with 1 mM $MgSO_4 \cdot 7H_2O$, 0.2% (w/v) glucose and 0.00005%
272 (w/v) thiamine. Solid substrates were prepared by adding 20 g/L of agar and were grown in a 37°C static
273 aerated incubator.

274 Solid growth substrates were also prepared with different nutritional profiles and agar concentrations to
275 quantify the resulting change in internal morphology of Δ*ompR* biofilms. No-salt agar substrates were
276 prepared without NaCl, and soft agar substrates were prepared by reducing the amount of agar to 10
277 g/L. D-Glucose was added to both LB and M9 media to final concentrations of 0.02% (w/v), 0.2% (w/v) or
278 0.5% (w/v).

279

280 ## 4.2.   Growth characterisation of BW25113 and Δ*ompR* in high osmolality
281 ## medium
282 The growth of the parental strain BW25113 and of the mutant strain Δ*ompR* in liquid medium were
283 characterised using a plate reader. LB broth was prepared with iodixanol concentrations of 0%, 1%, 2%,
284 5%, 10% and 20% (v/v) by adding appropriate amounts of an OptiPrep 60% (w/v) iodixanol stock
285 solution (Sigma-Aldrich, USA). Ten wells of a 96-well plate were then filled with 200 µL of medium with
286 each iodixanol concentration (corresponding to five biological replicates for each strain). Overnight
287 cultures of BW25113 and of the Δ*ompR* mutant strain were prepared in LB broth as described above and
288 were diluted to a starting OD_{600} of 0.01. The plate was then loaded with the lid on onto a pre-warmed
289 (37°C) Synergy HT plate reader (BioTek, USA), where the OD_{600} of the cultures was measured every 15
290 minutes for 24 hours while the plate was shaking continuously at medium speed.

291 Growth curves were plotted in Prism by exporting data from the Gen5 microplate software (BioTek,
292 USA), with the y axis plotted on a logarithmic scale. Specific growth rates were calculated as the slope of
293 the linear region of the semi-logarithmic plot using the equation

$$\mu = 2.303(log_{10}N - log_{10}N_0)/(t - t_0)$$

294 N_0 and N are the cell numbers at the beginning and at the end of the exponential growth phase,
295 respectively, and correspond to optical density readings, and t_0 and t are the times at which exponential
296 growth phase starts and ends, respectively [31].

297 To compare cell shape phenotype before and after growth in high osmolality medium, BW25113 and
298 Δ*ompR* were first grown as liquid cultures overnight in LB broth. They were then diluted 1:100 in both LB

299 broth and LB broth with 20% (v/v) iodixanol with LB salts increased proportionally, and were incubated
300 further in a 37°C aerated incubator while shaking at 250 rpm until mid-exponential growth phase,
301 before imaging using phase contrast microscopy as described below. Solid LB medium plates were
302 prepared with iodixanol concentrations of 1%, 10% and 20% (v/v), and used as substrates for the growth
303 of BW25113 and ΔompR biofilms.

304

4.3. Single-cell phase contrast microscopy

306 For single-cell imaging, overnight cultures of each strain in LB broth were diluted 1:100 and incubated
307 for two hours until they reached mid-exponential growth phase (OD_{600} = 0.4-0.6). Imaging slides were
308 prepared by sandwiching 1 mL of molten 1% agarose between two microscope slides and letting it
309 solidify at room temperature. After removing the top slide, 10 µL of liquid culture was spotted onto the
310 solidified agarose pads, and a coverslip was added prior to imaging. Single-cell phase contrast images
311 were acquired for both non-fluorescent strains (BW25113, BW25113 ΔamiA::kan, BW25113
312 ΔompR::kan, BW25113 ΔydgD::kan) and fluorescent strains (BW25113 / pAJR145, BW25113 ΔamiA::kan
313 / pAJR145, BW25113 ΔompR::kan / pAJR145, BW25113 ΔydgD::kan / pAJR145), to ensure that the
314 addition of chloramphenicol required for the maintenance of the pAJR145 plasmid did not affect the cell
315 phenotype of each strain.

316 Single cell imaging was carried out using an Eclipse E600 upright widefield microscope (Nikon, Japan) in
317 phase contrast mode equipped with a 100x/1.30 DLL oil immersion lens (Nikon, Japan). Illumination was
318 provided by a halogen lamp and the image was detected using a Hamamatsu ORCA 100 digital camera
319 (Hamamatsu, Japan).

320

4.4. Biofilm confocal microscopy

322 The GFP-expressing strains BW25113 / pAJR145, BW25113 ΔamiA::kan / pAJR145, BW25113
323 ΔompR::kan / pAJR145 and BW25113 ΔydgD::kan / pAJR145 were grown into mature biofilms on agar
324 substrates in a sterile 3D-printed plastic specimen holder, as described previously [16]. Biofilms were
325 grown for 24 hours when using LB medium, and for 48 hours when using M9 medium.

326 Mature biofilm images were acquired on an Olympus IX81 microscope coupled to a FluoView FV1000
327 confocal laser scanning unit (Olympus, Japan). Fluorescence from GFP was excited using a 488 nm argon
328 laser (GLG3135, Showa Optronics, Japan) and was detected by a PMT with a spectral detection window
329 set between wavelengths of 510 and 560 nm. Samples were imaged using a 10x/0.4 N.A. air objective
330 lens for resolving intra-colony channels.

331 Three-dimensional z-stacks of biofilms grown on LB and M9 media were acquired with a slice spacing of
332 5 µm for Nyquist sampling in the axial dimension. Five different colony biofilms were imaged for each
333 condition.

334

4.5. Image analysis

336 Phase-contrast images of both fluorescent and non-fluorescent cells were first pre-processed in FIJI
337 using the background subtraction tool with a rolling ball radius of 15 pixels, with the "light background"

338 option selected. The images were then analysed using the FIJI plugin MicrobeJ [32] to obtain cell length
339 and width measurements. Segmentation was performed using MicrobeJ with the default settings for a
340 bright background and the "medial axis" mode of detection. The following changes to the default
341 parameter ranges were made: area [1-max] μm^2; width [0-max] μm with variation [0-0.2]; sinuosity [1-
342 1.2]; angularity [0-0.5] rad; solidity [0.9-max]. The default "advanced" parameters were changed to have
343 an area cut-off of 1000, and a count cut-off of 250. The options "exclude on edges" and "shape
344 descriptors" were selected. Phase contrast images were analysed (n = 10 for each strain), with a total
345 number of analysed cells between 202 and 665 (non-fluorescent cells) and between 90 and 524
346 (fluorescent cells).

347 Biofilm image z-stacks were displayed as hyperstacks, and colour-coded by depth using the "fire" lookup
348 table on FIJI. Biofilms images were contrast-adjusted where needed for presentation purposes, using
349 Contrast Limited Adaptive Histogram Equalization (CLAHE, [33]) available in FIJI with block size 60,
350 maximum slope 3 and 256 histogram bins. Regions of interest (ROIs) in biofilm images were despeckled
351 using the "noise – despeckle" function in FIJI.

352

4.6.   Fractal complexity quantification

354 Fractal complexity was quantified using the FIJI plugin ComsystanJ (Complex Systems Analysis for
355 ImageJ) [34], version 1.0.0 (https://github.com/comsystan/comsystanj). The "2D image" version of the
356 plugin was used on the images, all of which had a size of 2048 x 2048 pixels. Box-counting fractal
357 dimension was calculated using the Relative Differential Box Counting (RDBC) algorithm developed by
358 Jin et al. [35] which uses a raster box scanning method. The plugin was run with 12 boxes and 1-12
359 regressions.

360 Firstly, four sets of sample images were analysed. Three of the sets were generated as grayscale images
361 through ComsystanJ using the "2D image Image Generator" option, with image types "Constant",
362 "Fractal random shapes – Lines" and "Random". Constant images had a constant pixel intensity value
363 (256) throughout each image. Line images were made of light (pixel intensity = 256) lines with varying
364 thickness randomly intersecting on a dark (pixel intensity = 0) background. Fractal images were obtained
365 from the "Wikimedia commons" open-source image repository [36]–[40]. Finally, in Random images
366 every pixel had a random intensity value (between 0 and 256).

367 For biofilm fractal pattern analysis, z-stacks were converted to 8-bit. No contrast-adjustment was used
368 on the images prior to analysis.

369

4.7.   Statistical analysis

371 Statistical tests were carried out on Prism version 8.0.2 (GraphPad Software, USA). Cell measurements
372 (length and width) of the mutant strains were compared to those of the parental strain BW25113 using
373 a Kruskal-Wallis multiple comparisons test. One-way ANOVA tests were used to compare box-counting
374 dimensions of biofilms formed by different strains in the same media and also to compare box-counting
375 dimensions of the same strain grown in different media.

376 In the main text and figure captions, values are presented as mean ± standard deviation. In all plots,
377 produced using Prism version 8.0.2, p-values are presented as * ($p < 0.05$); ** ($p < 0.005$); *** ($p < 0.0005$); **** ($p < 0.0001$), with specific p-values written in the figure captions.
378 0.0005); **** ($p < 0.0001$), with specific p-values written in the figure captions.

379

5. CRediT authorship contribution statement

381 **Beatrice Bottura**: Conceptualisation, Methodology, Validation, Formal Analysis, Investigation,
382 Resources, Data Curation, Writing – Original Draft, Writing – Review & Editing, Visualisation.
383 **Liam M. Rooney**: Conceptualisation, Methodology, Resources, Writing – Review & Editing.
384 **Morgan Feeney**: Methodology, Supervision, Writing – Review & Editing
385 **Paul A. Hoskisson**: Conceptualisation, Methodology, Writing – Review & Editing, Resources, Supervision,
386 Project Administration, Funding Acquisition.
387 **Gail McConnell**: Conceptualisation, Methodology, Writing – Review & Editing, Resources, Supervision,
388 Project Administration, Resources, Funding Acquisition.

389

6. Declaration of competing interest

391 The authors declare that they have no known competing financial interests or personal relationships
392 that could have appeared to influence the work reported in this paper.

393

7. Acknowledgements

405 For the purpose of open access, the author(s) has applied a Creative Commons Attribution (CC BY)
406 licence to any Author Accepted Manuscript version arising from this submission.

407

408

References

410 [1] B. L. Hogan, 'Morphogenesis', *Cell*, vol. 96, no. 2, pp. 225–233, 1999.

[2]   L. Eigentler, F. A. Davidson, and N. R. Stanley-Wall, 'Mechanisms driving spatial distribution of residents in colony biofilms: an interdisciplinary perspective', *Open Biol.*, vol. 12, no. 12, p. 220194, 2022.

[3]   M. Obert, P. Pfeifer, and M. Sernetz, 'Microbial growth patterns described by fractal geometry', *J. Bacteriol.*, vol. 172, no. 3, pp. 1180–1185, 1990.

[4]   S. Hermanowicz, U. Schindler, and P. Wilderer, 'Fractal structure of biofilms: new tools for investigation of morphology', *Water Sci. Technol.*, vol. 32, no. 8, pp. 99–105, 1995.

[5]   A. Moreau, G. Lorite, C. Rodrigues, A. Souza, and M. Cotta, 'Fractal analysis of Xylella fastidiosa biofilm formation', *J. Appl. Phys.*, vol. 106, no. 2, 2009.

[6]   H. Beyenal, C. Donovan, Z. Lewandowski, and G. Harkin, 'Three-dimensional biofilm structure quantification', *J. Microbiol. Methods*, vol. 59, no. 3, pp. 395–413, 2004.

[7]   T. Matsuyama and M. Matsushita, 'Self-similar colony morphogenesis by gram-negative rods as the experimental model of fractal growth by a cell population', *Appl. Environ. Microbiol.*, vol. 58, no. 4, pp. 1227–1232, 1992.

[8]   J. Wang, X. Li, R. Kong, J. Wu, and X. Wang, 'Fractal morphology facilitates Bacillus subtilis biofilm growth', *Environ. Sci. Pollut. Res.*, vol. 29, no. 37, pp. 56168–56177, 2022.

[9]   D. Tomoiaga, J. Bubnell, L. Herndon, and P. Feinstein, 'High rates of plasmid cotransformation in E. coli overturn the clonality myth and reveal colony development', *Sci. Rep.*, vol. 12, no. 1, pp. 1–15, 2022.

[10] I. N. Nuñez *et al.*, 'Artificial symmetry-breaking for morphogenetic engineering bacterial colonies', *ACS Synth. Biol.*, vol. 6, no. 2, pp. 256–265, 2017.

[11] T. J. Rudge, F. Federici, P. J. Steiner, A. Kan, and J. Haseloff, 'Cell polarity-driven instability generates self-organized, fractal patterning of cell layers', *ACS Synth. Biol.*, vol. 2, no. 12, pp. 705–714, 2013.

[12] M. Gralka, F. Stiewe, F. Farrell, W. Möbius, B. Waclaw, and O. Hallatschek, 'Allele surfing promotes microbial adaptation from standing variation', *Ecol. Lett.*, vol. 19, no. 8, pp. 889–898, 2016.

[13] J. Kayser, C. F. Schreck, Q. Yu, M. Gralka, and O. Hallatschek, 'Emergence of evolutionary driving forces in pattern-forming microbial populations', *Philos. Trans. R. Soc. B Biol. Sci.*, vol. 373, no. 1747, p. 20170106, 2018.

[14] B. Borer, D. Ciccarese, D. Johnson, and D. Or, 'Spatial organization in microbial range expansion emerges from trophic dependencies and successful lineages', *Commun. Biol.*, vol. 3, no. 1, p. 685, 2020.

[15] D. R. Amor, R. Montañez, S. Duran-Nebreda, and R. Solé, 'Spatial dynamics of synthetic microbial mutualists and their parasites', *PLoS Comput. Biol.*, vol. 13, no. 8, p. e1005689, 2017.

[16] L. M. Rooney, W. B. Amos, P. A. Hoskisson, and G. McConnell, 'Intra-colony channels in E. coli function as a nutrient uptake system', *ISME J.*, vol. 14, no. 10, pp. 2461–2473, 2020, doi: 10.1038/s41396-020-0700-9.

[17] B. Bottura, L. M. Rooney, P. A. Hoskisson, and G. McConnell, 'Intra-colony channel morphology in Escherichia coli biofilms is governed by nutrient availability and substrate stiffness', *Biofilm*, vol. 4, p. 100084, 2022.

[18] T. Ford, J. Graham, and D. Rickwood, 'Iodixanol: a nonionic iso-osmotic centrifugation medium for the formation of self-generated gradients', *Anal. Biochem.*, vol. 220, no. 2, pp. 360–366, 1994.

[19] S. Chakraborty and L. J. Kenney, 'A new role of OmpR in acid and osmotic stress in Salmonella and E. coli', *Front. Microbiol.*, vol. 9, p. 2656, 2018.

[20] J. M. Wood, 'Perspectives on: the response to osmotic challenges: bacterial responses to osmotic challenges', *J. Gen. Physiol.*, vol. 145, no. 5, p. 381, 2015.

[21] X. Dai and M. Zhu, 'High osmolarity modulates bacterial cell size through reducing initiation volume in Escherichia coli', *Msphere*, vol. 3, no. 5, pp. e00430-18, 2018.

[22] R. Buda *et al.*, 'Dynamics of Escherichia coli's passive response to a sudden decrease in external osmolarity', *Proc. Natl. Acad. Sci.*, vol. 113, no. 40, pp. E5838–E5846, 2016.

[23] E. Rojas, J. A. Theriot, and K. C. Huang, 'Response of Escherichia coli growth rate to osmotic shock', *Proc. Natl. Acad. Sci.*, vol. 111, no. 21, pp. 7807–7812, 2014.

[24] F. Li *et al.*, 'Effects of NaCl concentrations on growth patterns, phenotypes associated with virulence, and energy metabolism in Escherichia coli BW25113', *Front. Microbiol.*, vol. 12, p. 705326, 2021.

[25] Z. Ji, K. J. Card, and F. B. Dazzo, 'CMEIAS JFrad: a digital computing tool to discriminate the fractal geometry of landscape architectures and spatial patterns of individual cells in microbial biofilms', *Microb. Ecol.*, vol. 69, pp. 710–720, 2015.

[26] J. Kittler and J. Illingworth, 'Minimum error thresholding', *Pattern Recognit.*, vol. 19, no. 1, pp. 41–47, 1986.

[27] T. Baba *et al.*, 'Construction of Escherichia coli K-12 in-frame, single-gene knockout mutants: the Keio collection', *Mol. Syst. Biol.*, vol. 2, no. 1, pp. 2006–0008, 2006.

[28] K. A. Datsenko and B. L. Wanner, 'One-step inactivation of chromosomal genes in Escherichia coli K-12 using PCR products', *Proc. Natl. Acad. Sci.*, vol. 97, no. 12, pp. 6640–6645, 2000.

[29] A. J. Roe *et al.*, 'Co-ordinate single-cell expression of LEE4-and LEE5-encoded proteins of Escherichia coli O157: H7', *Mol. Microbiol.*, vol. 54, no. 2, pp. 337–352, 2004.

[30] K. L. Elbing and R. Brent, 'Recipes and tools for culture of Escherichia coli', *Curr. Protoc. Mol. Biol.*, vol. 125, no. 1, p. e83, 2019, doi: 10.1002/cpmb.83.

[31] A. K. Camper, G. A. McFeters, W. G. Characklis, and W. L. Jones, 'Growth kinetics of coliform bacteria under conditions relevant to drinking water distribution systems', *Appl. Environ. Microbiol.*, vol. 57, no. 8, pp. 2233–2239, 1991.

[32] A. Ducret, E. M. Quardokus, and Y. V. Brun, 'MicrobeJ, a tool for high throughput bacterial cell detection and quantitative analysis', *Nat. Microbiol.*, vol. 1, no. 7, pp. 1–7, 2016.

[33] K. Zuiderveld, 'Contrast limited adaptive histogram equalization', in *Graphics Gems*, Academic Press, 1994, pp. 474–485.

[34] H. Ahammer *et al.*, 'ComsystanJ: A collection of Fiji/ImageJ2 plugins for nonlinear and complexity analysis in 1D, 2D and 3D', *Plos One*, vol. 18, no. 10, p. e0292217, 2023.

[35] X. Jin, S. Ong, and others, 'A practical method for estimating fractal dimension', *Pattern Recognit. Lett.*, vol. 16, no. 5, pp. 457–464, 1995.

[36] 'Koch Curve in Three Dimensions ("Delta" fractal).jpg - Wikipedia'. 2014. Accessed: Nov. 16, 2023. [Online]. Available: https://commons.wikimedia.org/wiki/File:Koch_Curve_in_Three_Dimensions_(%22Delta%22_fractal).jpg

[37] 'Mandel zoom 00 mandelbrot set.jpg - Wikipedia'. 2013. Accessed: Nov. 16, 2023. [Online]. Available: https://commons.wikimedia.org/wiki/File:Mandel_zoom_00_mandelbrot_set.jpg

[38] 'BenMiriello/fun-with-fractals - GitHub Repository'. 2020. Accessed: Nov. 16, 2023. [Online]. Available: https://github.com/BenMiriello/fun-with-fractals

[39] 'Cubic starfish Julia set.png - Wikipedia'. 2021. Accessed: Nov. 16, 2023. [Online]. Available: https://commons.wikimedia.org/wiki/File:Cubic_starfish_Julia_set.png

[40] 'Xaos fractal 24.png - Wikipedia'. 2006. Accessed: Nov. 16, 2023. [Online]. Available: https://commons.wikimedia.org/wiki/File:Xaos_fractal_24.png